metals

MDPI

Article

Influence of Friction Stir Processing Post-Treatment on the Microstructure and Mechanical Properties of 205A Aluminum Alloy Produced by Wire Arc-Directed Energy Deposition

Jing Ma, Siyue Fan, Yuqi Gong, Qingwei Jiang * and Fei Li *

Faculty of Materials Science and Engineering, Kunming University of Science and Technology, Kunming 650093, China; mjing202202@163.com (J.M.); fansiyue2022@163.com (S.F.); 17693163989@163.com (Y.G.)
* Correspondence: jqw6@163.com (Q.J.); lifei06119@163.com (F.L.)

Abstract: Although wire arc-directed energy deposition (WA-DED) technology demonstrates advancements in the rapid manufacturing of high-strength Al-Cu aluminum alloy components, coarse microstructures and pore defects inhibit its further development and application. In this study, friction stir processing (FSP) post-treatment was employed to improve the microstructure and mechanical properties of the 205A aluminum alloy component produced by WA-DED, and the effects of rotational rate on the microstructure and properties were also investigated. Key findings showed that the average grain size of the as-deposited sample was significantly refined from 22.8 μm to less than 5 μm after FSP post-treatment, and most of the pore defects were eliminated. Most of the α-Al + θ-Al_2Cu eutectic structures distributed on the grain boundaries were dissolved into the α-Al matrix after FSP post-treatment, and the element segregation phenomenon was effectively improved. The microhardness of the stirred zone significantly increased due to the microstructure refinement and pore elimination. The excellent elongation of the component was obtained after FSP post-treatment using a relatively low rotational rate of 800 min^{-1}. Comparatively, after improving the rotational rate to 1200 min^{-1}, the strength of the component slightly increased with the reduction in elongation. Compared to the as-deposited sample, the average yield strength, ultimate tensile strength, and elongation increased by 32.7%, 20.6% and 56.7%, respectively.

Keywords: WA-DED; 205A aluminum alloy; FSP; microstructure; mechanical properties

check for updates

Academic Editors: Irene Buj Corral and Felip Fenollosa-Artés

Received: 20 February 2025
Revised: 13 March 2025
Accepted: 17 March 2025
Published: 19 March 2025

Citation: Ma, J.; Fan, S.; Gong, Y.; Jiang, Q.; Li, F. Influence of Friction Stir Processing Post-Treatment on the Microstructure and Mechanical Properties of 205A Aluminum Alloy Produced by Wire Arc-Directed Energy Deposition. *Metals* **2025**, *15*, 331. https://doi.org/10.3390/met15030331

Copyright: © 2025 by the authors. Licensee MDPI, Basel, Switzerland. This article is an open access article distributed under the terms and conditions of the Creative Commons Attribution (CC BY) license (https://creativecommons.org/licenses/by/4.0/).

1. Introduction

The wire arc-directed energy deposition (WA-DED) process utilizes an electric arc as a heat source and metal wire as raw materials to realize the integrated manufacturing of parts through layer-by-layer deposition [1]. WA-DED is increasingly being applied to the production of large components in the aerospace and automation fields due to the advantages of high deposition efficiency, excellent material utilization, and minimal limitations on the print size of the parts [2,3]. 205A, an Al-Cu-Mn series aluminum alloy, is popular for its essential lightweight structural components because of the low density, high specific strength, and good fracture toughness. Employing the WA-DED process to fabricate 205A aluminum alloy components not only enables the rapid achievement of desired outcomes but also contributes to a reduction in production costs [4].

However, the pore defects are inevitably introduced into the Al-Cu alloy component during WA-DED due to the poor weldability of the Al-Cu alloy [5]. Additionally, the rapid solidification and complex thermal cycle leads to the formation of coarse columnar grains

and heterogeneous microstructure [6]. These factors significantly weaken the mechanical properties of WA-DED components [7,8]. Numerous studies have been conducted to address the issues mentioned in previous research. A variety of methods have been used to modify the solidification of the melt pool during WA-DED, including cold metal transfer (CMT) technology [9,10], ultrasonic frequency pulses [11,12], applied magnetic fields [13,14], and assisted vibrations [15]. The application of new wires containing nano-sized TiC particles [16], Cd elements [17], Ti elements and Zr elements [18] is intended to promote the formation of fine equiaxed grains during solidification or the precipitation of strengthening phases during heat treatment. However, these strategies have limited influence on the pore defects.

The implementations of interlayer rolling [19], interlayer hammering [20], and interlayer (friction stir processing) FSP [21–23] during WA-DED offer an outstanding contribution in the improvement of pores defects and microstructure refinement. For example, Fang et al. [24] used the WA-DED + interlayer hammering process to prepare a 2219 aluminum alloy component (50.8% deformation). The microstructure was refined and the total volume of pore defects was reduced from 0.46 mm^3 to 0.12 mm^3, yielding a tensile strength of 334.6 MPa and elongation of 12.6%. The grain structures of the 2219 aluminum alloy component were significantly refined to 5.2 μm and tensile strength is increased from 249 MPa to 278 MPa using WA-DED + interlayer FSP process [21]. However, these interlayer processing methods are highly dependent on the equipment and increase the production cycle. In contrast, post-treatment processes such as FSP not only produce components with a fine microstructure, but are also beneficial for reducing production cost [25,26].

FSP is a process that improves the mechanical properties by refining the microstructure through severe plastic deformation [27]. In addition to serving as an interlayer process, FSP can be used as a post-treatment method [28,29]. According to Cui et al. [30], the grain size in the stirred zone of the WA-DED Al-Mg-Sc alloy was reduced to 2.4 μm after FSP post-treatment. Compared to the as-deposited (AD) sample, the tensile strength and elongation after FSP post-treatment were improved to 365 MPa and 24.8%, respectively. He et al. [31] also reported that the application of FSP post-treatment reduced the average grain size of WA-DED 6061 aluminum alloy from 128.3 μm to 5.1 μm and increased the average tensile strength from 234.5 MPa to 248.5 MPa in both horizontal and vertical directions. It is evident that the FSP post-treatment has a significant effect on the microstructure and mechanical properties of WA-DED aluminum alloys. Yu et al. [32] reported the effects of post-treatment FSP on the corrosion-resistant ZL205A aluminum alloy fabricated by WA-DED. The corrosion resistance of the WA-DED ZL205A alloy was significantly improved by FSP post-treatment. However, research on the effect of FSP post-treatment on the microstructure and mechanical properties of WA-DED 205A alloy is very limited in the existing literature. Consequently, it is necessary to explore the FSP post-treatment process for WA-DED Al-Cu alloys.

In this study, FSP post-treatment was employed to strengthen the WA-DED 205A aluminum alloy. The microstructures of the stirred zone were examined, and the mechanical properties of the samples were assessed both before and after processing. The effects of tool rotational rates on the microstructure and mechanical properties were also investigated.

2. Materials and Methods

In this study, the filler material is ER205A aluminum alloy wire with a diameter of 1.2 mm, and 6061-T6 aluminum alloy with a size of 300 mm × 300 mm × 16 mm is used as the substrate. Table 1 presents the chemical composition of the wire, component, and

substrate, which was determined using an inductively coupled plasma optical emission spectrometer (ICP-OES, Agilent 500, Santa Clara, CA, USA).

Table 1. The chemical composition of the wire, components and substrate (wt.%).

Alloys	Al	Cu	Mn	Mg	Si	Cd	Zr	Ti	V	Fe
Wire	Bal.	5.2	0.43	0.05	0.06	0.18	0.19	0.21	0.11	0.15
Component	Bal.	4.8	0.41	0.01	0.04	0.07	0.16	0.18	0.08	0.11
Substrate	Bal.	0.23	-	0.87	0.75	-	-	0.15	-	0.43

The component was deposited using the additive equipment Arcman S1 adv (Nanjing Enigma Industrial Automation Technology Co., Ltd., Nanjing, China), and the power supply type was Fronius TPS 4000 CMT ADV (Wels, Austria). A schematic of the WA-DED process is shown in Figure 1a. Pure argon (99.99%) was selected as the shielding gas during WA-DED, and the gas flow rate was 18 L/min. An interlayer residence time of 120 s was set to improve the forming quality. The deposition parameters are shown in Table 2.

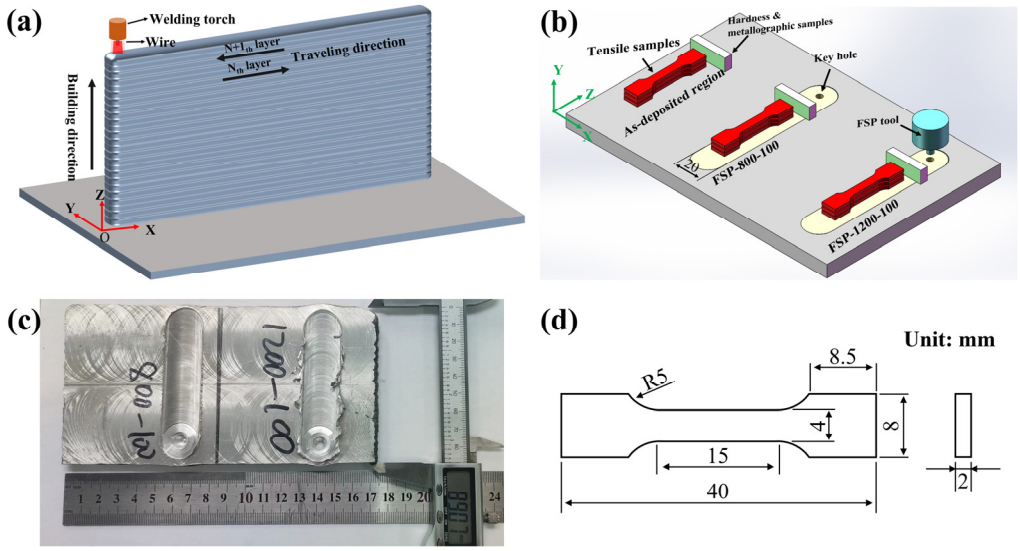

Figure 1. Schematic of (**a**) WA-DED process and (**b**) FSP post-treatment and the location of the experimental samples; (**c**) WA-DED Al-Cu-Mn alloy component after FSP post-treatment; (**d**) dimensions of the tensile specimen.

Table 2. Deposition parameters for WA-DED 205A aluminum alloy component.

Deposition Parameters	Values
I (A)	97
U (V)	16.9
Wire feeding speed (m/min)	4.9
Travel speed (mm/min)	320
Mode	Cold Metal Transfer + Pulse (CMT + P)

After WA-DED, a 205A alloy component with dimensions of 170 mm × 9 mm × 90 mm (length × width × height) was obtained. The thickness was reduced to 6.5 mm by milling, and a schematic diagram of FSP post-treatment is shown in Figure 1b. The WA-DED 205A component was fixed on the substrate, and FSP post-treatment was performed at the rotational rates of 800 min^{-1} and 1200 min^{-1} with a welding speed of 100 mm/min. A stirring tool featuring a shoulder diameter of 20 mm and a spiral V-shaped stirring pin

with a pin length of 6.3 mm was utilized. The tool tilt angle was set to 3° to the *Z*-axis of the machine during FSP. The components after FSP post-treatment are shown in Figure 1c. The treated parts were named as FSP-800-100 and FSP-1200-100, respectively, reflecting the respective rotational rates.

Metallographic, hardness, and tensile samples were prepared using wire electrical discharge machining (WEDM, Jiangsu Zhongte CNC Technology Co., Ltd., DK7750, Nanjing, China). The pulse width, pulse interval, current, and voltage in WEDM were set to 32 μs, 35 μs, 2 A, and 100 V, respectively. The microstructure was analyzed using an optical microscope (OM, Nikon Eclipse Ma200, Tokyo, Japan), a scanning electron microscope (SEM, ZEISS EVO 18 Research, Oberkochen, Germany) equipped with energy dispersive spectroscopy (EDS, Bruker XFlash 6130, Billerica, MA, USA), and an X-ray diffractometer (XRD, Rigaku MiniFlex 600, Tokyo, Japan). Keller's reagent was used to etch the metallographic samples. A microhardness tester (Laizhou Heng Yi Testing Instrument Co., HVS-1000AT, Yantai, China) was used to perform microhardness tests under a load of 200 g and a holding time of 10 s. The interval was 0.5 mm, and the result was the average of 12 test values. The room temperature tensile test was performed by a universal material testing machine (MTS-E45, Eden Prairie, MN, USA) with a strain rate of 0.001 s^{-1}. Three tensile specimens were taken for each condition. The dimensions of the tensile specimen are shown in Figure 1d. Thermo-Calc software 2024b, developed by Thermo-Calc Software AB in Solna, Sweden, is a professional tool for thermodynamic calculations of materials. In this study, it was utilized to calculate the Scheil solidification sequence of the Al-4.8Cu-0.41Mn-0.18Ti-0.16Zr aluminum alloy. Grain size and porosity statistics were analyzed using ImageJ 1.54f software, developed by the National Institutes of Health (NIH) in Bethesda, USA.

3. Results and Discussion

3.1. Macrostructure and Microstructure

Figure 2 shows the microstructure of AD samples. The microstructure of the YOZ cross-section is composed of fine equiaxed grains distributed in the interlayer and coarse columnal grains and equiaxed grains within the inner layer (Figure 2a). The average grain sizes are 22.3 μm in the interlayer and 76.2 μm in the inner layer, respectively, as illustrated in Figure 3a,b. The microstructure in the XOY section is composed of coarse and fine equiaxed grains, with an average grain size of 43.8 μm (Figure 3c). The grain structures in the two sections indicate that the microstructure of the alloy is inhomogeneous. The inhomogeneous microstructure distribution is related to the deposition characterization during WA-DED [33]. The equilibrium phase diagram of the Al-4.8Cu-0.41Mn-0.18Ti-0.16Zr aluminum alloy is provided in Figure 4. During solidification, the precipitation temperature of Al_3Zr and Al_3Ti phases is considered to be above 924.5 K, and then α-Al phases precipitate by consuming liquid phases. In the final stage, the eutectic reaction happens at 817.4 K until the liquid phase is depleted. High-melting-point Al_3Ti and Al_3Zr phases formed prior to the α-Al grains during solidification possess very similar crystal structures and lattice parameters to the α-Al phases, which are considered as the effective nuclei of α-Al to refine grain structures [34]. Therefore, fine equiaxed grains are mainly formed in the interlayer because this zone meets the nucleation condition of fine equiaxed grains that includes enough nuclei and high supercooling. In the inner layer, heat dissipation is relatively slow as compared to the interlayer, and grain growth in the same direction as the temperature gradient becomes dominant, resulting in the formation of coarse columnar grains.

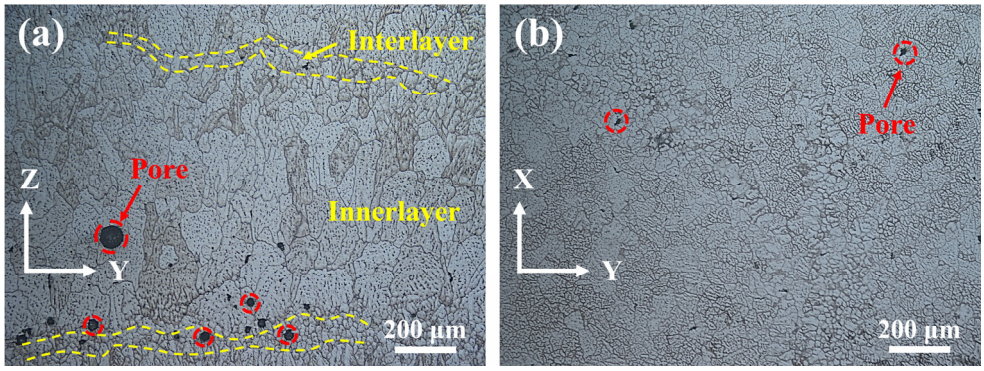

Figure 2. Microstructure of the AD sample: (**a**) YOZ cross-section; (**b**) XOY cross-section.

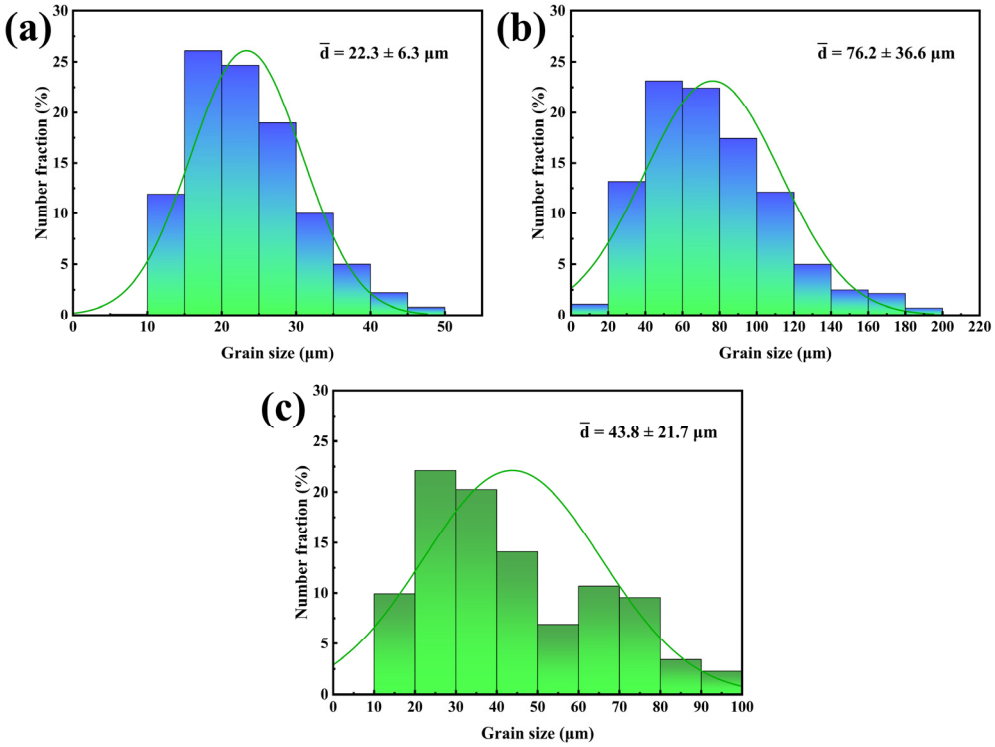

Figure 3. Grain size: (**a**) interlayer region and (**b**) inner layer region for YOZ cross-section; (**c**) XOY cross-section.

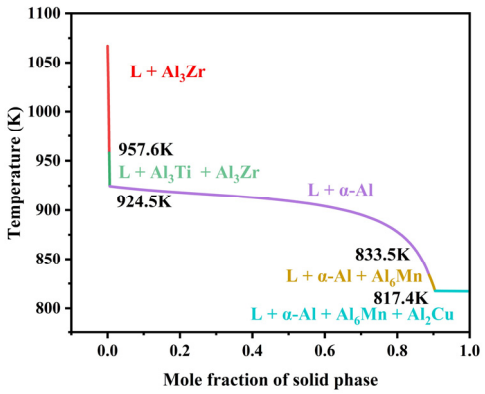

Figure 4. Scheil solidification sequence diagram of Al-4.8Cu-0.41Mn-0.18Ti-0.16Zr (wt.%) alloy calculated using Thermo-Cacl 2024b software.

In addition, pore defects are primarily observed in the interlayer. This phenomenon is associated with the precipitation, upward floating and escape of hydrogen during solidification due to solubility differences between solid and liquid Al [35,36]. The pores have an adverse effect on the mechanical properties. Particularly, large size pores are formed in the component. The area percentage of the pores in Figure 2 was calculated, and the results indicated that the percentage of pores in the AD samples was 0.63%.

The macrostructure of the XOY cross-section in the FSP-800-100 sample is shown in Figure 5. Five distinct zones can be identified: the shoulder-driven zone (SDZ), the pin-driven zone (PDZ), thermo-mechanically affected zone (TMAZ), heat-affected zone (HAZ), and base material (BM). Meanwhile, the SDZ and PDZ collectively constitute the nugget zone (NZ). A distinct "onion ring" structure is found in the PDZ, which is formed by the periodic rotation of stirring pin. Evidently, all pore defects are eliminated in the NZ and TMAZ.

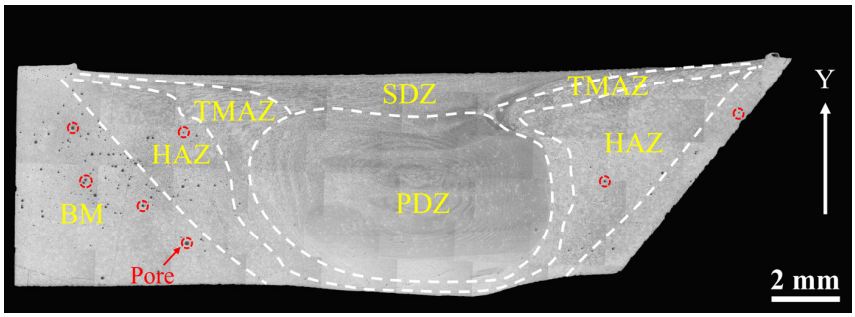

Figure 5. Macrostructure of FSP-800-100 sample (XOY cross-section).

Figure 6 shows the microstructure of each zone in the FSP-800-100 sample. The microstructure of SDZ consists of fine equiaxed grains with an average grain size of 4.3 μm, as shown in Figure 6a. The grain sizes are increased as the distance from the shoulder increases. The component top is strongly deformed due to its proximity to the shoulder, and the grain structures are significantly refined. It is different from SDZ, as the microstructure of PDZ is composed entirely of fine equiaxed grains of uniform size (Figure 6b).

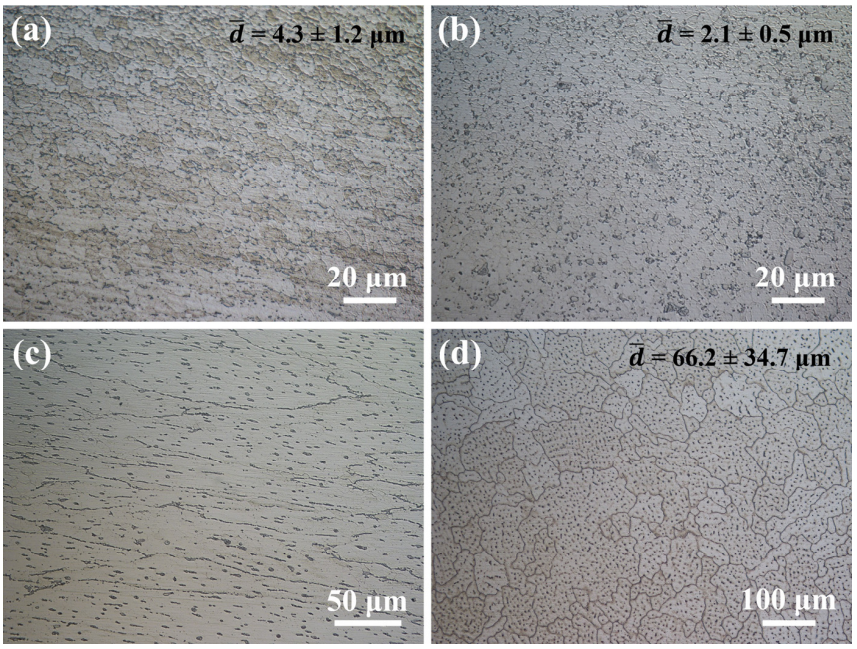

Figure 6. Microstructure of different zones in the FSP-800-100 sample: (**a**) SDZ; (**b**) PDZ; (**c**) TMAZ; (**d**) HAZ.

In the TMAZ, grain structures are elongated in a certain direction, which depends on the direction of the force applied to the materials when it is agitated (Figure 6c). The formation of TMAZ originates from the material flows of plasticized materials provided by the high rotational movement of the stirring tool. The grain size along the elongation direction is more than 100 μm.

In HAZ, the thermal cycling during the FSP process increased the average grain size to 66.2 μm, as shown in Figure 6d.The macrostructure of the FSP-1200-100 sample is illustrated in Figure 7, and the detailed microstructures are shown in Figure 8. The microstructures are similar between FSP-800-100 and FSP-1200-100 samples, but more coarse grain structures are obtained in the FSP-1200-100 sample. The coarsening of grain structures is related to the increase in rotational rate. The "onion ring" is distinct, which indicates that stronger plastic deformation happened in the FSP-1200-100 sample.

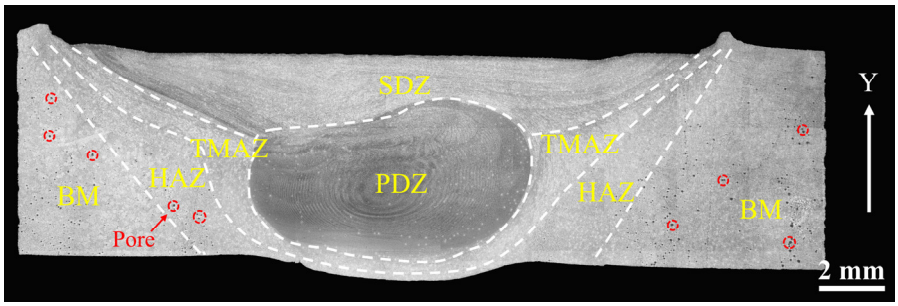

Figure 7. Macrostructure of FSP-1200-100 sample (XOY cross-section).

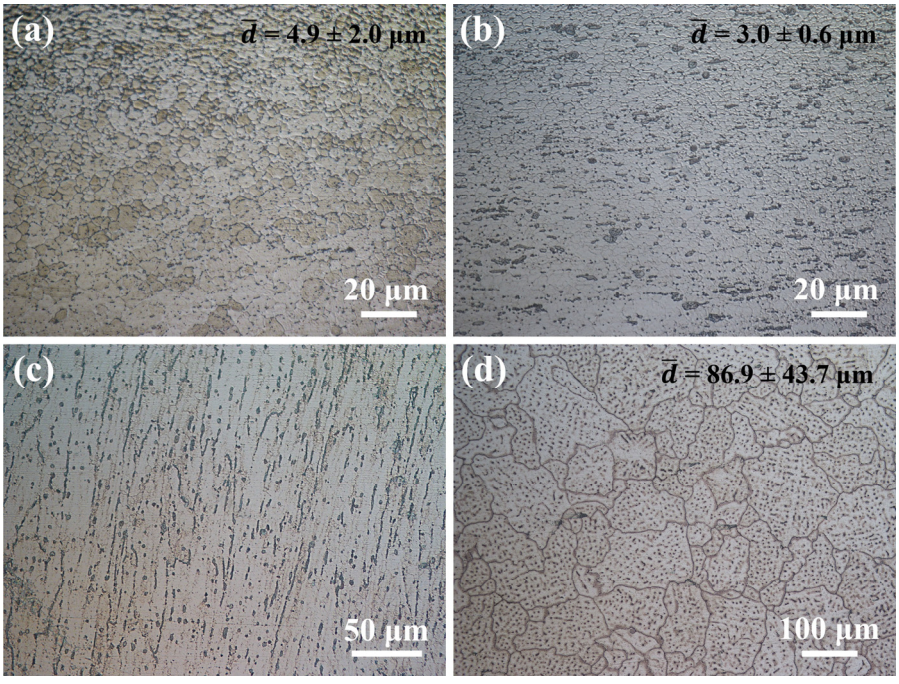

Figure 8. Microstructure of different zones in the FSP-1200-100 sample: (**a**) SDZ; (**b**) PDZ; (**c**) TMAZ; (**d**) HAZ.

After FSP post-treatment, grain structures of the component in the stirred zone are significantly refined. The continuous dynamic recrystallization (CDRX) [37–39] is the primary mechanism of microstructure evolution. During FSP, severe plastic deformation and thermal effects occur in the stirring zone [40]. High-density dislocations are introduced by plastic deformation to form subgrains characterized by a high density of dislocations and

internal stress. Meanwhile, the dynamic recovery of dislocations also happens under the effect of friction heat [41]. These subgrains consistently absorb the dislocations and rotate to accommodate the strain incompatibility of neighboring subgrains until the formation of fine recrystallization grains occurs. During FSP, the microstructure is restructured under violent plastic deformation, and the pore defects are effectively eliminated by material flow. Additionally, the recrystallization grain sizes are related to the rotational rate of the stirring tool. Applying a high rotational rate of 1200 min^{-1} can increase heat input, causing the coarsening of grain structures.

3.2. Second Phase

The SEM images and EDS results of the AD samples, FSP-800-100 samples and FSP-1200-100 samples are presented in Figure 9. In the AD sample, grain structures are composed of coarse equiaxed grains. The SEM images and corresponding EDS point-scan results demonstrate that the eutectic structure (α-Al + Al_2Cu) precipitates continuously at the grain boundaries (GBs) (point A_1) and sporadically within the grains in an irregular shape (points A_2 and A_3).

After FSP-800-100, grain structures of SDZ are significantly refined and most of α-Al + Al_2Cu (Points B_1–B_3) are dissolved into the α-Al matrix, as depicted in Figure 9b. Compared to the SDZ, PDZ exhibits a finer grain structure, but the dissolution of α-Al + Al_2Cu (Points C_1–C_3) is lower (Figure 9c). The heat generated by the friction between the shoulder and the workpiece during the FSP process accounts for 70% to 80% of the total heat, while the remaining heat is produced by the rotation of the stirring pin [42]. The coarsening of the grains in the SDZ is attributed to the high heat input and slow heat dissipation. However, a high temperature promotes more dissolution of second phases. Comparatively, lower heat generation in the PDZ can refine grain structures but inhibit dissolution of second phases to a certain degree.

Figure 9d,e show the microstructure of SDZ and PDZ in the FSP-1200-100 sample. By increasing the rotational rate to 1200 min^{-1}, grain structures are coarsened due to the increase in heat input. However, better dissolution of α-Al + Al_2Cu (Points D_1–D_3) occurs in the FSP-1200-100 sample. In the SDZ, almost of α-Al + Al_2Cu (Points E_1–E_3) are dissolved into the α-Al matrix.

The EDS results are provided in Figure 9f–j. The distribution of Cu, as the primary alloying element in Al-Cu alloys, is particularly important. In the AD sample, Cu elements are mainly enriched on the GBs, leading to the segregation of Cu atoms (Figure 9f). The segregation of Cu atoms can be attributed to the fact that the purer metal crystallizes first during solidification, causing the solute Cu atoms to be expelled outward and ultimately solidify with Al to form a Cu-rich eutectic structure [6]. However, the segregation of Cu atoms is significantly improved after FSP post-treatment, which suggests that more homogeneous microstructures are obtained.

Figure 10 provides the XRD patterns of different samples. All samples are composed of α-Al and θ-Al_2Cu phases. In addition, the content of the (111) crystallographic plane increased significantly in the FSP-treated samples, while the contents of the (200), (220), (311), and (222) planes exhibited a notable decrease. These changes in the peak intensity of α-Al may be associated with alterations in microstructure due to the FSP treatment. Since the slip system of the Al-Cu alloy at room temperature is {111} <110> [43], the increase in the (111) crystallographic plane is also a manifestation of the improvement in plasticity after FSP in subsequent experiments.

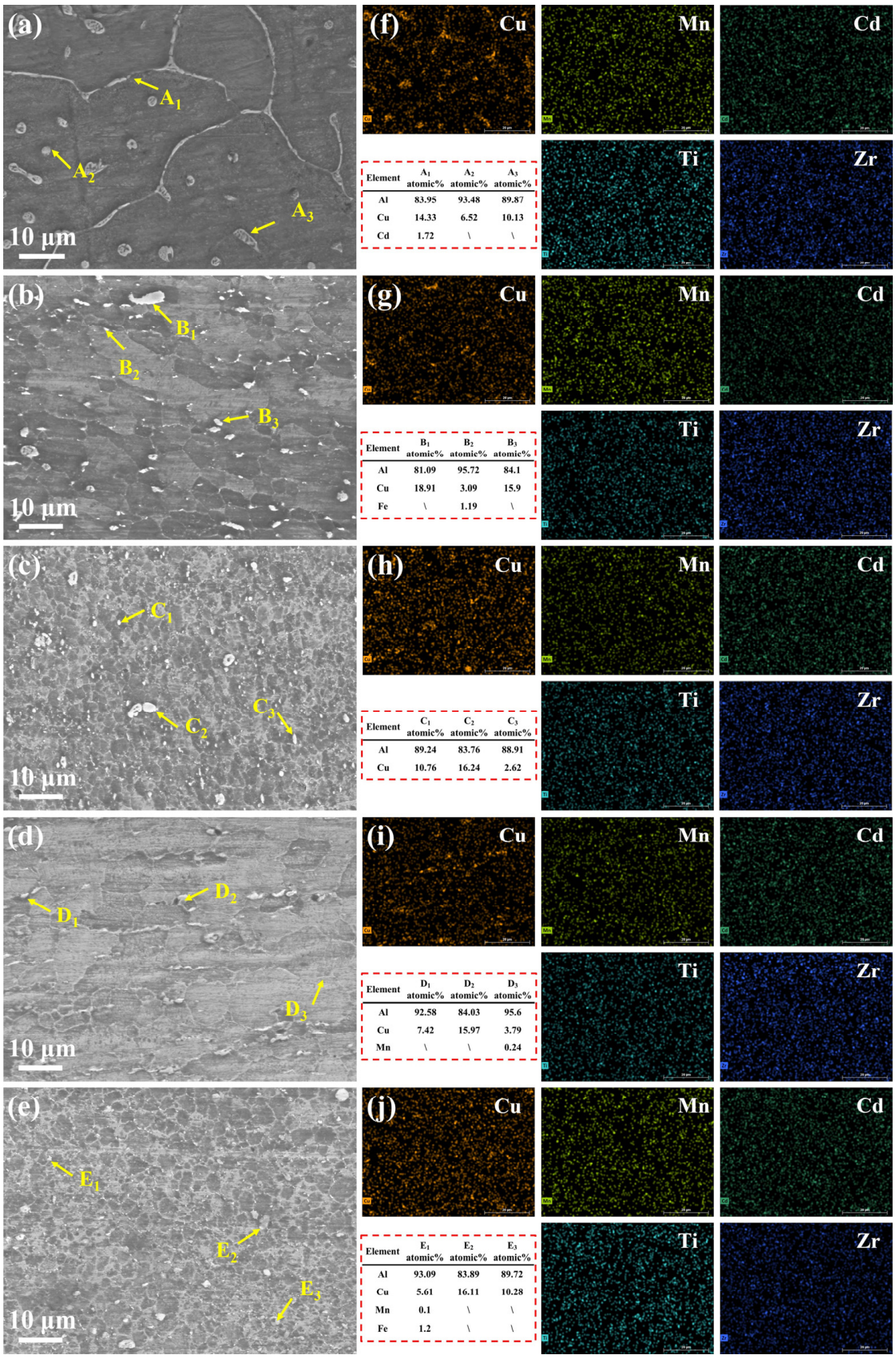

Figure 9. SEM images and EDS maps of (**a**,**f**) AD sample, (**b**,**g**) SDZ of FSP-800-100 sample, (**c**,**h**) PDZ of FSP-800-100 sample, (**d**,**i**) SDZ of FSP-1200-100 sample, (**e**,**j**) PDZ of FSP-1200-100 sample.

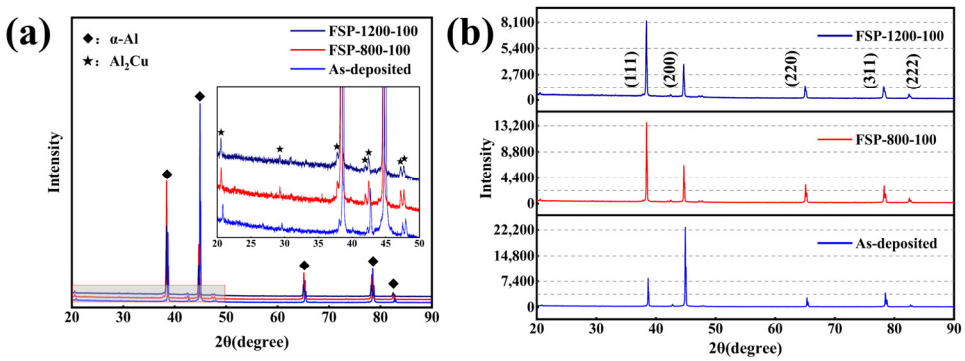

Figure 10. XRD patterns of (**a**) AD sample, FSP-800-100 sample, and FSP-1200-100 sample, and (**b**) comparison of the α-Al peak intensities among the three samples.

3.3. Mechanical Properties

3.3.1. Microhardness

In the *X*-axis direction, hardness gradually decreases from SDZ to BM. In the *Y*-axis direction, the microhardness value of PDZ is obviously higher than that of SDZ. This difference in hardness is primarily attributed to variations in grain size and phases. The average microhardness of PDZ is the highest, reaching a Vickers hardness (HV) value of 82.1, which represents a 14.4% increase compared to that of the AD sample.

In accordance with the observed trends in hardness variations across different regions of the FSP-800-100 sample, the SDZ in the FSP-1200-100 sample exhibited the highest average microhardness of 82.7 HV, followed by the PDZ of 80.4 HV, while the BM recorded the lowest microhardness at 70.8 HV.

According to Figures 11 and 12, the average microhardness of the FSP-treated samples increased significantly, as compared to the AD samples (BM). The most notable increase in microhardness was observed in the FSP-800-100 and FSP-1200-100 samples for the PDZ, which both exhibited an increase of over 14.4% compared to the BM, with the SDZ demonstrating the second most significant increase. This enhancement in microhardness following FSP can be attributed to several factors, grain refinement, elimination of porosity, and the fragmentation and dissolution of the coarse eutectic structure. The observed discrepancy between excessive heat and increased plastic deformation at 1200 min^{-1} explains why the average microhardness of the SDZ and PDZ in the FSP-1200-100 samples is not significantly different from that of the FSP-800-100 samples.

3.3.2. Tensile Properties

Figure 13 demonstrates the tensile properties of the samples before and after FSP post-treatment. As shown in Figure 13a, the samples exhibited higher yield strength (YS), ultimate tensile strength (UTS), and elongation (EL) after FSP post-treatment. Additionally, the tensile curves of the three types of samples displayed distinct sawtooth-like fluctuations during the plastic deformation stage. This phenomenon, known as the Portevin-Le Chatelier effect, is a common occurrence of plastic instability in aluminum alloys. The occurrence of this phenomenon is linked to the dynamic interaction between solute atoms and dislocations during deformation [44].

In Figure 13b, the YS, UTS, and EL of the AD sample are 113 MPa, 227 MPa and 14.1%, respectively. The average YS after various FSP treatments remains relatively consistent, showing an increase of approximately 32.3% compared to the AD samples. In contrast, the UTS of the FSP-800-100 and FSP-1200-100 samples is increased by 21.1% and 23.3%, respectively, while the EL is improved by 56.7% and 48.9% compared to that of the AD sample.

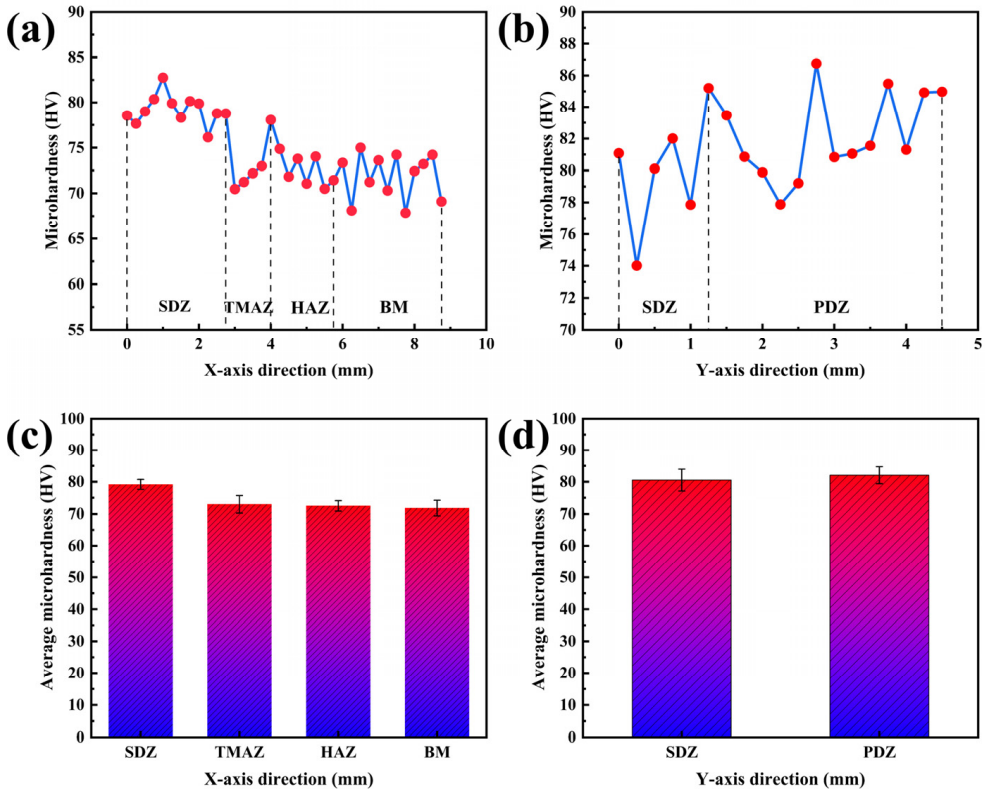

Figure 11. Hardness distribution and average hardness of SDZ, TMAZ, HAZ and BM in the FSP-800-100 sample: (**a**,**c**) *X*-axis direction; (**b**,**d**) *Y*-axis direction.

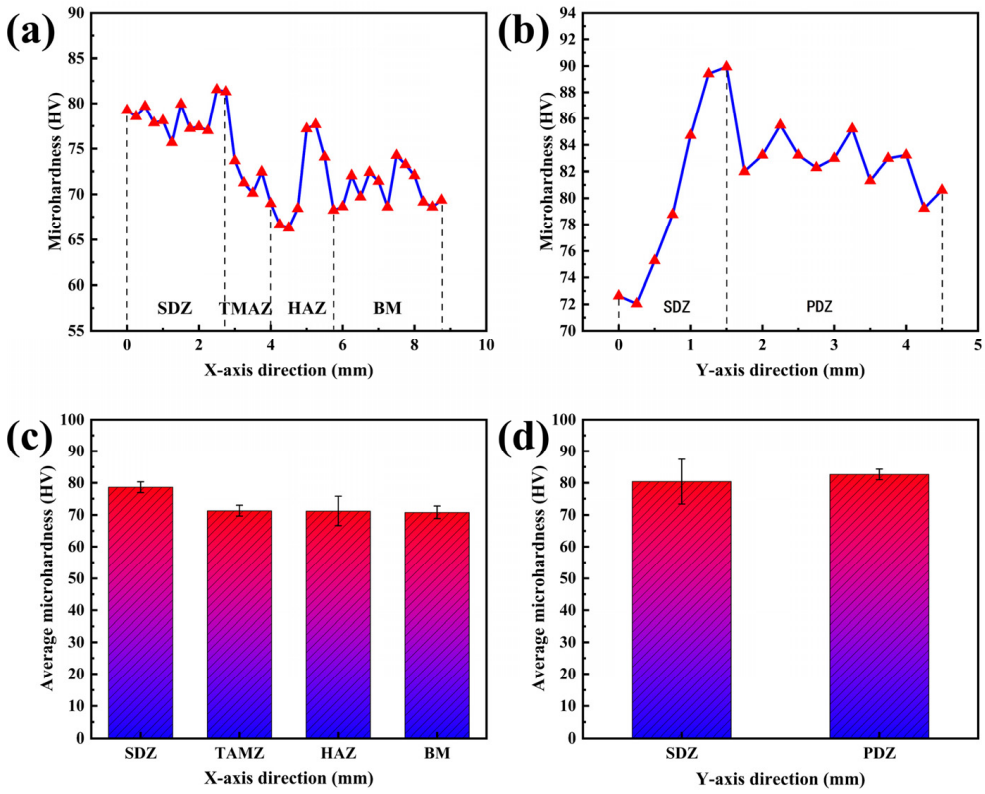

Figure 12. Hardness distribution and average hardness of SDZ, TMAZ, HAZ and BM in the FSP-1200-100 sample: (**a**,**c**) *X*-axis direction; (**b**,**d**) *Y*-axis direction.

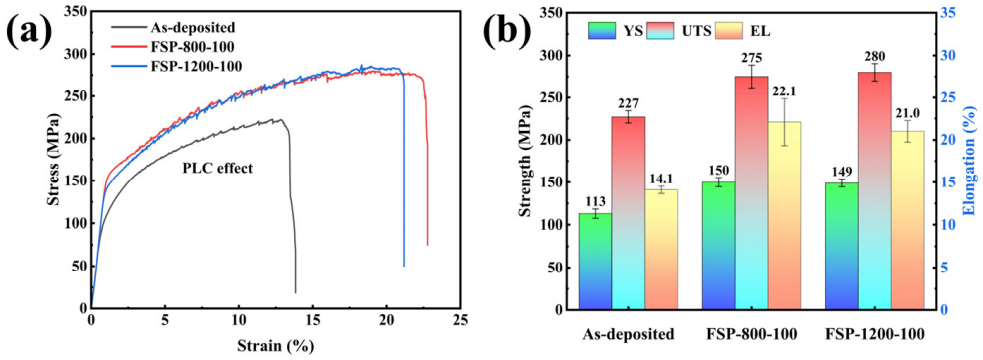

Figure 13. Tensile testing results of AD samples, FSP-800-100 samples, and FSP-1200-100 samples: (**a**) engineering stress–strain curves; (**b**) tensile properties (note: the three curves in Figure 13a are from one of the three tensile specimens in the corresponding state).

The increase in tensile properties after FSP treatment can be attributed to grain refinement, elimination of pores, and the dissolution of the coarse eutectic structure into the Al matrix. During tensile testing, grain refinement enhances the number of grains that facilitate dislocation glide, allowing deformation to be distributed among individual grains. This distribution reduces stress concentration, thereby increasing the extent of plastic deformation [45]. The presence of pores diminishes the load-bearing area of the material in the AD sample and these pores are primarily located in the interlayer region, reducing the tensile properties of the material. Once the pores are eliminated, the material experiences uniform deformation. Furthermore, the coarse eutectic structure, initially a weak point in the deformation process, is fragmented by FSP and integrated into the matrix, further enhancing tensile properties [46].

As illustrated in Figures 6a,b and 8a,b, a fine grain structure was achieved in the NZ region following the FSP treatment. However, it is evident that the grain sizes in the SDZ and PDZ of the FSP-1200-100 samples are larger compared to those in the FSP-800-100 samples. The higher rotational speed during the FSP process induces more intense plastic deformation of the microstructures, which facilitates grain refinement and the dissolution of coarse eutectic structures into the α-Al matrix, thereby enhancing the tensile properties. However, the increase in rotational speed also results in greater frictional heat, which can lead to grain coarsening. This contradiction explains why the FSP-1200-100 sample did not achieve superior tensile properties compared to the FSP-800-100 sample.

3.3.3. Fracture Analysis

The fracture morphologies of different samples are shown in Figure 14. The fracture surface of the AD sample shows poor fracture flatness, indicating the inhomogeneity of the microstructure (Figure 14a). Meanwhile, the numerous pores on the fracture surface (Figure 14a) demonstrate the porous microstructure of the AD sample. In Figure 14b, many equiaxed dimples can be observed and many second phases are distributed at the bottom of the dimples. According to dislocation theory, the reduction in bonding strength between these granular second phases and the matrix during stretching is responsible for the initial formation of the dimples [47,48]. Additionally, the formation of pores reduces the carrying capacity of the materials during tensile testing, reducing the mechanical properties of the AD sample.

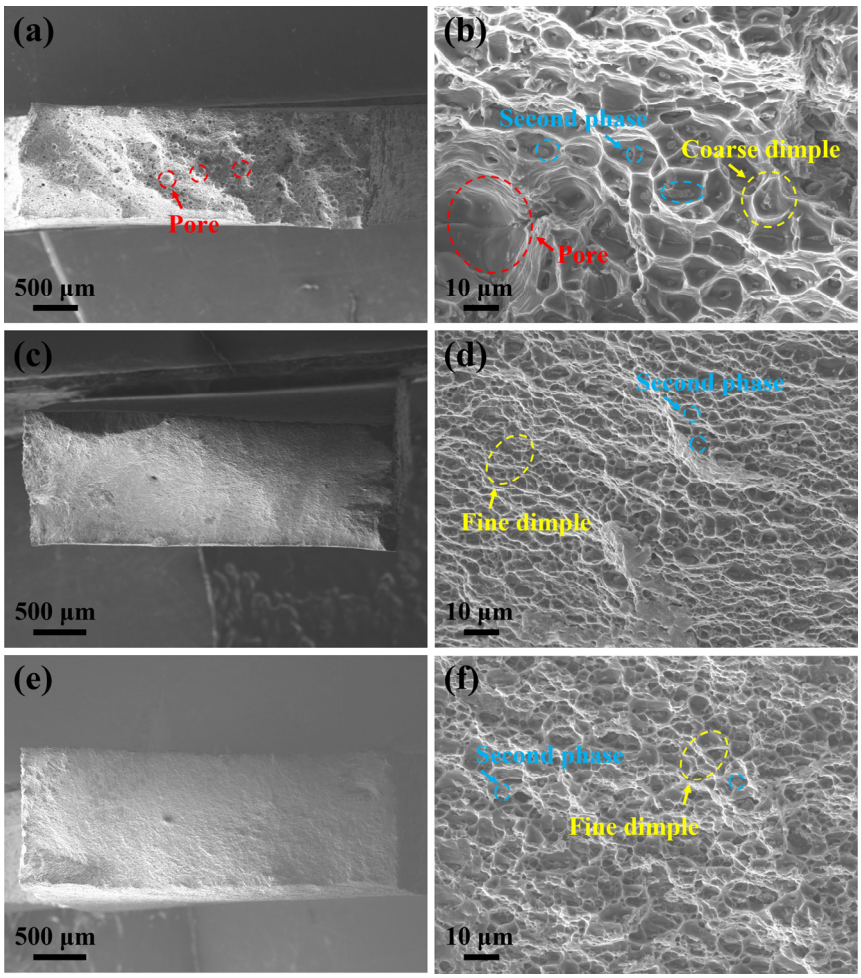

Figure 14. Macro-morphology and micro-morphology of tensile fracture: (**a**,**b**) AD sample, (**c**,**d**) FSP-800-100 sample; (**e**,**f**) FSP-1200-100 sample.

In the FSP-800-100 sample, no pores are seen in the fracture surface, and the fracture is relatively flat (Figure 14c). The results suggest that the pore defects can be effectively eliminated by FSP post-treatment. The heat generated by friction during the FSP process softens the alloy, which facilitates a vigorous stirring process that leads to significant thermoplastic flow (i.e., substantial plastic deformation) in the stirred region, resulting in the reconstruction of the microstructure. Additionally, porosity is eliminated during this process [49,50].

The dissolution and homogeneous distribution of the original second phases following FSP post-treatment are critical factors in achieving the fine equiaxed dimple features. The fracture surface of the FSP-1200-100 samples is illustrated in Figure 14e,f. In comparison to the FSP-800-100 sample, the variability in equiaxed dimple size within the micro-morphology has increased. The increased grain size caused by the higher rotational rate explains the changes in dimple size. Compared to the AD samples, the changes in microstructure after FSP treatment made them less prone to necking during stretching, which promoted the formation of more dimples. However, the connection between dimples through shear fracture resulted in smaller and shallower dimples. Additionally, the slight decrease in elongation of the FSP-1200-100 sample, compared to the FSP-800-100 sample, is also reflected in the small increase in its dimple size.

4. Conclusions

In this study, the FSP post-treatment process was applied to improve the microstructure and mechanical properties of the WA-DED 205A aluminum alloy component. The following conclusions can be drawn:

(1) The microstructure of the AD sample consists of coarse columnar grains and equiaxed grains, which exhibited a broad range of size distribution. This inhomogeneous microstructure reduces the mechanical properties of the component.

(2) After FSP, the grain structure in the stirred zone transforms into fine recrystallized grains, and pore defects are effectively eliminated. Compared to a rotation speed of 800 min^{-1}, a rotation speed of 1200 min^{-1} leads to more intense plastic deformation and a higher degree of dissolution of the second phase. However, the increased heat input associated with the higher rotation rate also leads to an increase in grain size.

(3) The mechanical properties of the component were significantly enhanced after FSP post-treatment. The highest average microhardness values for the FSP-800-100 and FSP-1200 samples were recorded at 82.1 HV and 82.7 HV, respectively. The tensile strength for these samples reached 275 MPa and 280 MPa, representing an increase of over 21% compared to that of the AD samples. The elongation of FSP-800-100 and FSP-1200 samples is 22.1% and 21.0%, respectively, which is more than 50% higher than that of the AD sample. The slight difference in strength between the two processing speeds can be attributed to the conflict between the dissolution of the second phase and grain coarsening at a higher rotational rate.

Author Contributions: Conceptualization, Q.J. and F.L.; methodology, J.M., S.F. and Y.G.; validation, Q.J. and F.L.; formal analysis, Q.J. and F.L.; investigation, J.M., S.F. and Y.G.; resources, S.F., Q.J. and F.L.; data curation, J.M., S.F. and Y.G.; writing—original draft preparation, J.M.; writing—review and editing, S.F., Q.J. and F.L.; supervision, Q.J. and F.L.; project administration, Q.J. and F.L.; funding acquisition, Q.J. and F.L. All authors have read and agreed to the published version of the manuscript.

Funding: This research was funded by the National Natural Science Foundation of China (Grant No. 52402077), National Natural Science Foundation of China under contract (Grant No. 51201077) and Yunnan fundamental research projects (202201AT070192, 202101BE070001-011).

Data Availability Statement: The original contributions presented in this study are included in the article. Further inquiries can be directed to the corresponding author.

Conflicts of Interest: The authors declare no conflicts of interest.

References

1. Blakey-Milner, B.; Gradl, P.; Snedden, G.; Brooks, M.; Pitot, J.; Lopez, E.; Leary, M.; Berto, F.; du Plessis, A. Metal additive manufacturing in aerospace: A review. *Mater. Des.* **2021**, *209*, 110008. [CrossRef]
2. Rodrigues, T.A.; Duarte, V.; Miranda, R.M.; Santos, T.G.; Oliveira, J.P. Current Status and Perspectives on Wire and Arc Additive Manufacturing (WAAM). *Materials* **2019**, *12*, 1121. [CrossRef] [PubMed]
3. Williams, S.W.; Martina, F.; Addison, A.C.; Ding, J.; Pardal, G.; Colegrove, P. Wire + Arc Additive Manufacturing. *Mater. Sci. Technol.* **2016**, *32*, 641–647. [CrossRef]
4. Tawfik, M.M.; Nemat-Alla, M.M.; Dewidar, M.M. Enhancing the properties of aluminum alloys fabricated using wire + arc additive manufacturing technique—A review. *J. Mater. Res. Technol.* **2021**, *13*, 754–768. [CrossRef]
5. Wu, B.T.; Pan, Z.X.; Ding, D.H.; Cuiuri, D.; Li, H.J.; Xu, J.; Norrish, J. A review of the wire arc additive manufacturing of metals: Properties, defects and quality improvement. *J. Manuf. Process.* **2018**, *35*, 127–139. [CrossRef]
6. Fan, S.Y.; Guo, X.M.; Li, Z.H.; Ma, J.; Li, F.; Jiang, Q.W. A Review of High-Strength Aluminum-Copper Alloys Fabricated by Wire Arc Additive Manufacturing: Microstructure, Properties, Defects, and Post-processing. *J. Mater. Eng. Perform.* **2023**, *32*, 8517–8540. [CrossRef]
7. Xue, C.P.; Zhang, Y.X.; Mao, P.C.; Liu, C.M.; Guo, Y.L.; Qian, F.; Zhang, C.; Liu, K.; Zhang, M.; Tang, S.Y.; et al. Improving mechanical properties of wire arc additively manufactured AA2196 Al–Li alloy by controlling solidification defects. *Addit. Manuf.* **2021**, *43*, 102019. [CrossRef]

8. Zhou, Y.H.; Lin, X.; Kang, N.; Wang, Z.N.; Tan, H.; Huang, W.D. Hot deformation induced microstructural evolution in local-heterogeneous wire + arc additive manufactured 2219 Al alloy. *J. Alloys Compd.* **2021**, *865*, 158949. [CrossRef]
9. Fang, X.W.; Chen, G.P.; Yang, J.N.; Xie, Y.; Huang, K.; Lu, B.H. Wire and Arc Additive Manufacturing of High-Strength Al–Zn–Mg Aluminum Alloy. *Front. Mater.* **2021**, *8*, 656429. [CrossRef]
10. Gierth, M.; Henckell, P.; Ali, Y.; Scholl, J.; Bergmann, J.P. Wire Arc Additive Manufacturing (WAAM) of Aluminum Alloy AlMg5Mn with Energy-Reduced Gas Metal Arc Welding (GMAW). *Materials* **2020**, *13*, 2671. [CrossRef]
11. Cong, B.Q.; Cai, X.Y.; Qi, Z.W.; Qi, B.J.; Zhang, Y.T.; Zhang, R.Z.; Guo, W.; Zhou, Z.G.; Yin, Y.H.; Bu, X.Z. The effects of ultrasonic frequency pulsed arc on wire + arc additively manufactured high strength aluminum alloys. *Addit. Manuf.* **2022**, *51*, 102617. [CrossRef]
12. Kuang, X.C.; Qi, B.; Zheng, H. Effect of pulse mode and frequency on microstructure and properties of 2219 aluminum alloy by ultrahigh-frequency pulse Metal-Inert Gas Welding. *J. Mater. Res. Technol.* **2022**, *20*, 3391–3407. [CrossRef]
13. Zhao, X.S.; Wang, Y.X.; Song, H.; Huang, J.W.; Zhang, H.O.; Chen, X.; Huang, C.; Li, R.S. Effect of auxiliary longitudinal magnetic field on overlapping deposition of wire arc additive manufacturing. *Int. J. Adv. Manuf. Technol.* **2023**, *125*, 1383–1401. [CrossRef]
14. Hu, Y.N.; Chen, F.R.; Cao, S.L.; Fan, Y.F.; Xie, R.J. Preparation and characterization of CMT wire arc additive manufacturing Al-5%Mg alloy depositions through assisted longitudinal magnetic field. *J. Manuf. Process.* **2023**, *101*, 576–588. [CrossRef]
15. Ma, C.; Li, C.; Yan, Y.; Liu, Y.; Wu, X.; Li, D.; Jin, H.; Zhang, F. Investigation of In Situ Vibration During Wire and Arc Additive Manufacturing. *3D Print Addit. Manuf.* **2023**, *10*, 524–535. [CrossRef]
16. Jin, P.; Liu, Y.B.; Li, F.X.; Li, J.Z.; Sun, Q.J. Realization of structural evolution in grain boundary, solute redistribution and improved mechanical properties by adding TiCnps in wire and arc additive manufacturing 2219 aluminium alloy. *J. Mater. Res. Technol.* **2021**, *11*, 834–848. [CrossRef]
17. Li, K.; Yang, T.B.; Hou, X.R.; Ji, C.; Zhu, L.; Li, B.X.; Cao, Y.; Zhao, L.; Ma, C.Y.; Tian, Z.L. Microstructure evolution and mechanical properties of Al–Cu–Mn–Cd alloy fabricated by CMT-wire arc additive manufacturing. *Mater. Sci. Eng. A* **2024**, *898*, 146395. [CrossRef]
18. Rakesh, M.; Srivastava, N.; Bhagavath, S.; Karagadde, S. Role of In Situ Formed (Al_3Zr + Al_3Ti) Particles on Nucleation of Primary Phase in Al-5 wt.% Cu Alloy. *J. Mater. Eng. Perform.* **2023**, *33*, 6488–6498. [CrossRef]
19. Gu, J.L.; Wang, X.S.; Bai, J.; Ding, J.L.; Williams, S.; Zhai, Y.C.; Liu, K. Deformation microstructures and strengthening mechanisms for the wire+arc additively manufactured Al-Mg4.5Mn alloy with inter-layer rolling. *Mater. Sci. Eng. A* **2018**, *712*, 292–301. [CrossRef]
20. Zhou, S.Y.; Wang, J.Y.; Yang, G.; Wu, B.; Xie, H.; Wu, K.; An, D. Periodic microstructure of Al–Mg alloy fabricated by inter-layer hammering hybrid wire arc additive manufacturing: Formation mechanism, microstructural and mechanical characterization. *Mater. Sci. Eng. A* **2022**, *860*, 144314. [CrossRef]
21. Wei, J.X.; He, C.S.; Qie, M.F.; Li, Y.; Zhao, Y.; Qin, G.W.; Zuo, L. Microstructure refinement and mechanical properties enhancement of wire-arc additive manufactured 2219 aluminum alloy assisted by interlayer friction stir processing. *Vacuum* **2022**, *203*, 111264. [CrossRef]
22. Qie, M.F.; Wei, J.X.; He, C.S. Microstructure evolution and mechanical properties of wire-arc additive manufactured Al–Zn–Mg–Cu alloy assisted by interlayer friction stir processing. *J. Mater. Res. Technol.* **2023**, *24*, 2891–2906. [CrossRef]
23. He, C.S.; Wei, J.X.; Li, Y.; Zhang, Z.Q.; Tian, N.; Qin, G.W.; Zuo, L. Improvement of microstructure and fatigue performance of wire-arc additive manufactured 4043 aluminum alloy assisted by interlayer friction stir processing. *J. Mater. Sci. Technol.* **2023**, *133*, 183–194. [CrossRef]
24. Fang, X.W.; Zhang, L.J.; Chen, G.P.; Huang, K.; Xue, F.; Wang, L.; Zhao, J.Y.; Lu, B.H. Microstructure evolution of wire-arc additively manufactured 2319 aluminum alloy with interlayer hammering. *Mater. Sci. Eng. A* **2021**, *800*, 140168. [CrossRef]
25. Chang, T.X.; Fang, X.W.; Liu, G.; Zhang, H.K.; Huang, K. Wire and arc additive manufacturing of dissimilar 2319 and 5B06 aluminum alloys. *J. Mater. Sci. Technol.* **2022**, *124*, 65–75. [CrossRef]
26. Zhou, Y.; Chang, T.X.; Fang, X.W.; Chen, R.K.; Li, Y.F.; Huang, K. Tailoring the mechanical properties and thermal stability of additive manufactured micro-alloyed Al-Cu alloy via multi-stage heat treatment. *Mater. Des.* **2023**, *233*, 112287. [CrossRef]
27. Zhou, S.Y.; Wu, K.; Yang, G.; Wu, B.; Qin, L.Y.; Guo, X.P.; Wang, X.M. Friction stir welding of wire arc additively manufactured 205A aluminum alloy: Microstructure and mechanical properties. *Mater. Sci. Eng. A* **2023**, *876*, 145154. [CrossRef]
28. Santos Macías, J.G.; Elangeswaran, C.; Zhao, L.; Van Hooreweder, B.; Adrien, J.; Maire, E.; Buffière, J.-Y.; Ludwig, W.; Jacques, P.J.; Simar, A. Ductilisation and fatigue life enhancement of selective laser melted AlSi10Mg by friction stir processing. *Scr. Mater.* **2019**, *170*, 124–128. [CrossRef]
29. Deng, Q.C.; Wu, Y.J.; Su, N.; Chang, Z.Y.; Chen, J.; Peng, L.M.; Ding, W.J. Influence of friction stir processing and aging heat treatment on microstructure and mechanical properties of selective laser melted Mg-Gd-Zr alloy. *Addit. Manuf.* **2021**, *44*, 102036. [CrossRef]

30. Cui, J.Y.; Guo, X.P.; Hao, S.; Guo, X.M.; Xu, R.Z. Achieving high strength-ductility properties of wire-arc additive manufactured Al-Mg-Sc aluminum alloy via friction stir processing post-treatment and high temperature aging treatment. *Mater. Lett.* **2023**, *350*, 134913. [CrossRef]
31. He, P.; Bai, X.W.; Zhang, H.O. Microstructure refinement and mechanical properties enhancement of wire and arc additively manufactured 6061 aluminum alloy using friction stir processing post-treatment. *Mater. Lett.* **2023**, *330*, 133365. [CrossRef]
32. Yu, L.; Wang, L.; Zhao, Y.; Wang, W.Y. Fabrication of corrosion-resistant ZL205A aluminum alloys thin-wall using WAAM: Exploring the synergistic effects of FSP and multidimensional nanomaterials. *J. Alloys Compd.* **2025**, *1016*, 178987. [CrossRef]
33. Fan, S.Y.; Guo, X.P.; Tang, Y.; Guo, X.M. Microstructure and Mechanical Properties of Al-Cu-Mg Alloy Fabricated by Double-Wire CMT Arc Additive Manufacturing. *Metals* **2022**, *12*, 416. [CrossRef]
34. Advanced Engineering MaterialsFan, S.Y.; Guo, X.M.; Jiang, Q.W.; Li, Z.H.; Ma, J. Microstructure Evolution and Mechanical Properties of Ti and Zr Micro-Alloyed Al-Cu Alloy Fabricated by Wire + Arc Additive Manufacturing. *JOM* **2023**, *75*, 4115–4127. [CrossRef]
35. Ryan, E.M.; Sabin, T.J.; Watts, J.F.; Whiting, M.J. The influence of build parameters and wire batch on porosity of wire and arc additive manufactured aluminium alloy 2319. *J. Mater. Process. Technol.* **2018**, *262*, 577–584. [CrossRef]
36. Toda, H.; Hidaka, T.; Kobayashi, M.; Uesugi, K.; Takeuchi, A.; Horikawa, K. Growth behavior of hydrogen micropores in aluminum alloys during high-temperature exposure. *Acta. Mater.* **2009**, *57*, 2277–2290. [CrossRef]
37. Yu, P.F.; Wu, C.S.; Shi, L. Analysis and characterization of dynamic recrystallization and grain structure evolution in friction stir welding of aluminum plates. *Acta. Mater.* **2021**, *207*, 116692. [CrossRef]
38. Khan Md, F.; Panigrahi, S.K. Achieving excellent thermal stability and very high activation energy in an ultrafine-grained magnesium silver rare earth alloy prepared by friction stir processing. *Mater. Sci. Eng. A* **2016**, *675*, 338–344. [CrossRef]
39. Singh, A.; Sharma, S.K.; Batish, A. Dynamic recrystallization during solid state friction stir welding/processing/additive manufacturing: Mechanisms, microstructure evolution, characterization, modeling techniques and challenges. *Crit. Rev. Solid State Mater. Sci.* **2025**, *50*, 77–135. [CrossRef]
40. Liu, X.C.; Ye, T.; Li, Y.Z.; Pei, X.J.; Sun, Z. Quasi-in-situ characterization of microstructure evolution in friction stir welding of aluminum alloy. *J. Mater. Res. Technol.* **2023**, *25*, 6380–6394. [CrossRef]
41. Jata, K.V.; Semiatin, S.L. Continuous dynamic recrystallization during friction stir welding of high strength aluminum alloys. *Scr. Mater.* **2000**, *43*, 743–749. [CrossRef]
42. Meng, X.C.; Huang, Y.X.; Cao, J.; Shen, J.J.; dos Santos, J.F. Recent progress on control strategies for inherent issues in friction stir welding. *Prog. Mater. Sci.* **2021**, *115*, 100706. [CrossRef]
43. Šebek, F.; Kubík, P.; Hůlka, J.; Petruška, J. Strain hardening exponent role in phenomenological ductile fracture criteria. *Eur. J. Mech. A-Solids* **2016**, *57*, 149–164. [CrossRef]
44. Jiang, H.F.; Zhang, Q.C.; Chen, X.D.; Chen, Z.J.; Jiang, Z.Y.; Wu, X.P.; Fan, J.H. Three types of Portevin–Le Chatelier effects: Experiment and modelling. *Acta Mater.* **2007**, *55*, 2219–2228. [CrossRef]
45. Liu, X.D.; Ye, L.Y.; Tang, J.G.; Ke, B.; Dong, Y.; Chen, X.J.; Gu, Y. Superplastic deformation mechanisms of a fine-grained Al–Cu–Li alloy. *Mater. Sci. Eng. A* **2022**, *848*, 143403. [CrossRef]
46. Gu, J.L.; Yang, S.L.; Gao, M.J.; Bai, J.; Zhai, Y.C.; Ding, J.L. Micropore evolution in additively manufactured aluminum alloys under heat treatment and inter-layer rolling. *Mater. Des.* **2020**, *186*, 108288. [CrossRef]
47. Fang, J.X.; Zhu, Z.Y.; Zhang, X.Q.; Xie, L.L.; Huang, Z.Y. Tensile Deformation and Fracture Behavior of AA5052 Aluminum Alloy under Different Strain Rates. *J. Mater. Eng. Perform.* **2021**, *30*, 9403–9411. [CrossRef]
48. Li, L.; Du, F.S. Effects of Sinusoidal Vibration of Crystallization Roller on Microstructure and Mechanical Properties of Ti/Al Laminated Composites by Twin-Roll Casting. *Trans. Indian Inst. Met.* **2023**, *76*, 2073–2083. [CrossRef]
49. Mo, S.; Zhang, Y.C.; Liu, Y.H.; Liu, W.B.; Zhou, Y.S.; Zhang, J.L.; Zhang, W. Nonlinear vibration and super-harmonic resonance analysis of aluminum alloy friction stir welding. *Nonlinear Dyn.* **2024**, *112*, 11013–11041. [CrossRef]
50. Choi, S.; Shim, D.; Kim, H. Reduction of Defects by Friction Stir Processing for Additively Manufactured Cast Aluminum Alloys (AlSiMg). *Int. J. Precis. Eng. Manuf.-Green Technol.* **2023**, *11*, 1193–1205. [CrossRef]

Disclaimer/Publisher's Note: The statements, opinions and data contained in all publications are solely those of the individual author(s) and contributor(s) and not of MDPI and/or the editor(s). MDPI and/or the editor(s) disclaim responsibility for any injury to people or property resulting from any ideas, methods, instructions or products referred to in the content.